Energy and AI 24 (2026) 100687

Contents lists available at ScienceDirect

Energy and AI

journal homepage: www.elsevier.com/locate/egyai

Data-driven machine learning modelling for the manufacturing of the fuel electrode support in solid oxide cells

Tan Le-Dinh [a,b,c], Hartmut Schlenz [c,d,*], Norbert H. Menzler [c], Alejandro A. Franco [a,b,e,f], Olivier Guillon [c,g]

[a] Laboratoire de Réactivité et de Chimie des Solides, UMR CNRS 7314, Université de Picardie Jules Verne, F-80039, Amiens Cedex 1, France
[b] Réseau sur le Stockage Electrochimique de l'Energie (RS2E), Hub de l'Energie, FR CNRS 3459, 15 rue Baudelocque, 80039 Amiens Cedex, France
[c] Forschungszentrum Jülich GmbH, Institute of Energy Materials and Devices (IMD), IMD-2: Materials Synthesis and Processing, 52428 Jülich, Germany
[d] Institute of Geoscience, Division of Geochemistry and Petrology, University of Bonn, Meckenheimer Allee 139, D-53115 Bonn, Germany
[e] ALISTORE-European Research Institute, Hub de l'Energie, FR CNRS 3104, 15 rue Baudelocque, 80039 Amiens Cedex, France
[f] Institut Universitaire de France, 103 boulevard Saint Michel, 75005 Paris, France
[g] Jülich Aachen Research Alliance: JARA-Energy, Jülich 52425, Germany

GRAPHICAL ABSTRACT

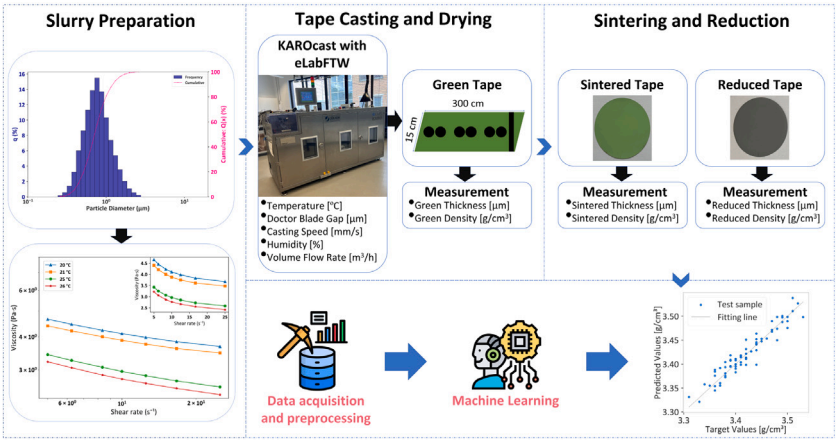

ARTICLE INFO

Keywords:
Solid oxide cells
Fuel-electrode substrate
Tape casting
Machine learning

ABSTRACT

The industry-relevant fabrication of supports in fuel-electrode supported Solid Oxide Cells (SOCs) by tape casting typically involves a multi-stage process, demanding precise control over tape thickness and density. However, conventional SOC manufacturing processes are resource-intensive and often rely on industry/R&D unpublished knowledge and trial-and-error practices to achieve the target properties of the resulting tape. Hence, machine learning (ML) was employed for predicting the thickness and density across three distinct stages of the fabrication process: tape casting, sintering, and NiO-reduction process. Our developed ML models (e.g., Extra Trees and Ridge Regressions) demonstrate exceptional accuracy (R^2 > 0.9) for each specific prediction task. Concurrently, experimental data analysis was conducted to elucidate the impact of the manufacturing parameters on the tape properties. Our data-driven ML approach offers a pathway towards achieving precise tape property control and advancing more efficient SOC support manufacturing.

* Corresponding author at: Forschungszentrum Jülich GmbH, Institute of Energy Materials and Devices (IMD), IMD-2: Materials Synthesis and Processing, 52428 Jülich, Germany.
E-mail address: h.schlenz@fz-juelich.de (H. Schlenz).

https://doi.org/10.1016/j.egyai.2026.100687
Received 31 October 2025; Received in revised form 31 December 2025; Accepted 20 January 2026
Available online 29 January 2026

1. Introduction

Hydrogen technologies have a pivotal role to play in the transition from fossil fuels to renewable energy, essential for realising net-zero and sustainable development plans [1,2]. Amongst these, solid oxide cells (SOCs) have emerged as one of the most promising technologies for clean energy conversion, offering high efficiency and versatile fuel flexibility [3–5]. Particularly, fuel electrode-supported SOCs (FESCs) offer an important advantage such as a thinner electrolyte layer (5–20 μm) [6–8]. This results in the reduction of ohmic losses, enabling lower operating temperatures (500–750 °C) and higher performance [9,10]. The mechanical stability of the FESCs is fundamentally dependent on the thick porous fuel-electrode support. The porous fuel-electrode support is typically made of NiO/Yttria-stabilised zirconia cermets [11, 12].

Tape casting is a well-known fabrication technique to produce thin ceramic sheets from ceramic slurry [13–15]. Since tape casting is potentially cost-efficient for mass production, this technique is preferable to produce SOC components [16–18]. To produce a high-quality green tape of the cermet-based support, traditional optimisation commonly relies on trial-and-error [19–21], leading to significantly substantial resource and time expenditure. The precise control of green tape thickness is crucial for governing the properties of the final tape-cast product [22,23]. In this regard, predicting the thickness and density of the tape obtained after drying is of the utmost importance in supporting the optimisation of the tape casting process. Nevertheless, the manufacturing process for the fuel-electrode support necessitates careful control over numerous relevant parameters such as temperature, doctor blade gap, casting speed, humidity, and exhaust air volume flow rate, as these directly influence the resulting green tape properties, indirectly impacting the tape during subsequent heat treatment stages. Such complex relationships are difficult to reproduce by using physico-chemical models, especially when drying and sintering need to be considered.

Alternatively, machine learning (ML) offers a powerful approach for this prediction task by learning from the data describing the complex manufacturing process, including tape casting and subsequent heat treatment processes such as sintering and reduction. This data-driven machine learning surrogate approach can predict a broad spectrum of material properties without requiring a fundamental understanding of their underlying chemistry or physics [24,25]. The application of ML-based techniques has recently achieved remarkable success in various fields of materials and energy sciences [26–34], including predicting material activity and properties [35–37], aiding new material discovery [38–40], driving material design [41–43], and analysing electrochemical energy device manufacturing [44–48]. These successes are achieved through the high quality of the dataset used in the relevant research. Effective data collection strategies are, therefore, critical for further advancing these applications, particularly within the context of data-driven manufacturing of SOCs. To ensure comprehensive and systematic data management in our research, an electronic laboratory notebook (ELN) was utilised in our work. Specifically, eLabFTW [49], a free and open-source electronic lab notebook, was implemented with a new Application Programming Interface (API) to enhance data traceability. This integration allows manufacturing parameters, routinely recorded in the machine's log files, to be directly and systematically transferred into eLabFTW. This automated process facilitates comprehensive and structured data management for our research. By leveraging the data-driven approach combining ML, the tape properties can be predicted for each fabrication stage in our study. We developed a modular ML approach to model the complex manufacturing process of the FESC support by training and evaluating separate predictive models on experimental data. This approach enables us to independently and accurately assess the predictability of the ML models, mitigating the forecast error accumulation across each stages [50,51].

Table 1
Raw materials used to prepare the casting slurry.

Material	Function	Supplier
NiO	Powder	G. Vogler B.V.
8YSZ	Powder	Imerys
Ethanol	Solvent	Merck
Methyl ethyl ketone	Solvent	Merck
Polyvinyl butyral B-98	Binder	Solutia Inc.
Solusolv S-2075	Plasticiser	Solutia Inc.
PEG400	Plasticiser	Merck
BYK 220 S	Dispersant	BYK

In this work, we propose a data-driven ML modelling framework to predict tape properties throughout the fabrication process of the fuel-electrode support, encompassing tape casting including drying, sintering, and reduction processes. To the best of our knowledge, this is the first ML-based data simulation workflow of the SOC fuel-electrode support manufacturing processes so as to predict the thickness and density of the support at each fabrication stage. Our workflow is shown in Fig. 1, in which the terms green thickness/density denote the thickness and density of the sample after drying, and reduced thickness/density refer to the corresponding values measured after the NiO-to-Ni reduction stage. Our study aims to develop a comprehensive understanding and predictive capability for the multi-stage fabrication process of the fuel-electrode supports. By combining rigorous semi-automated data collection with ML techniques, our novel approach using experimental data provides valuable insights about the direct influence of manufacturing parameters on the tape thickness and density throughout the tape casting stage, indirectly impacting the tape during subsequent sintering and reduction steps.

2. Materials and methods

2.1. Slurry preparation and rheological measurements

In this study, an optimised slurry formulation was used for all tape casting experiments. This means that the slurry composition, including solid loading and solvent content, was kept constant throughout the manufacturing of the fuel-electrode support. This formulation was previously developed and validated by Wolfgang Schafbauer, Norbert H. Menzler, and Hans P. Buchkremer [52]. Specifically, NiO (Green Nickel Oxide) and 8YSZ (8 mol% white yttria-stabilised zirconia) were used as the starting materials for the fuel electrode support to prepare the solvent-based slurry. A mixture of NiO and 8YSZ (57 : 43 volume fraction) was mixed with Ethanol, Methyl ethyl ketone, binders, dispersants, and plasticisers in the mixer for 10 h. The ceramic powders, organic materials and solvents used for the slurry preparation are listed in Table 1. The particle size distributions of NiO and 8YSZ were indistinguishable in the final prepared slurry and determined by d_{10} = 0.35–0.45 μm, d_{50} = 0.5–0.7 μm, and d_{90} = 0.8–1.0 μm. Fig. 2 further illustrates the detailed particle size distribution of the ceramic powder mixture in the prepared slurry.

It should be noted that slurry formulation parameters, such as solid content and solvent ratio, also play a critical role in tape casting. However, our reported approach is currently using the single, optimised slurry formulation when producing the support tape to ensure process stability and reproducibility. It also helped to avoid defects such as cracking or mechanical failure during subsequent thermal treatments (sintering and reduction), which are commonly encountered when varying slurry formulations. By using the optimised slurry formulation, the present work isolates the impact of environmental and equipment-related parameters (e.g., temperature, humidity, exhaust air volume flow rate, doctor blade gap, and casting speed) upon the resulting tape thickness and density.

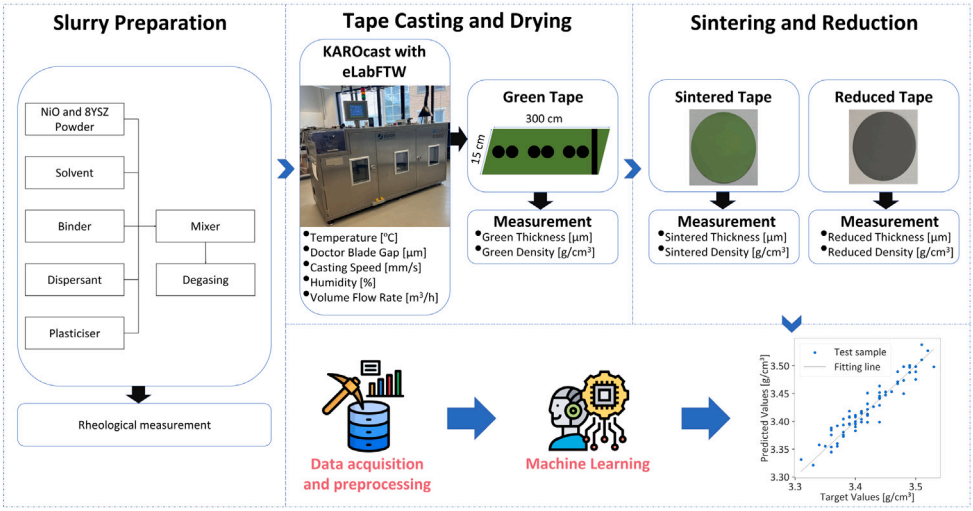

Fig. 1. Schematic workflow of a data-driven machine learning framework for the manufacturing process of the fuel-electrode support. Firstly, we prepared the slurry and implemented the slurry viscosity measurement. Then, we performed the tape casting to collect the data. The green tape was sintered and reduced after its measurement. The data was collected experimentally and preprocessed to construct a dataset for the SOC support fabrication process. The dataset was utilised to train and test different ML models to select the best fitting model and the respective hyperparameter fine-tuning for each prediction task.

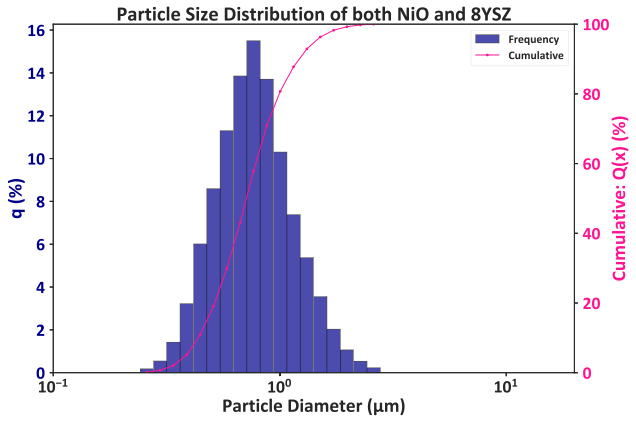

Fig. 2. Particle size distribution of both NiO and 8YSZ in the casting slurry. The primary y-axis on the left displays the frequency distribution (q(%)), showing the percentage of particles within a specific range of diameters. The secondary y-axis on the right-hand side represents the cumulative distribution ($Q(x)$ (%)), indicating the total percentage of particles with a diameter smaller than a given size. The particle diameter is plotted on a logarithmic scale (x-axis, µm).

The rheological behaviour of the slurry was investigated using a rotational rheometer (Physica MCR 301, Anton Paar GmbH, Austria) equipped with a coaxial cylinder measurement setup (CC27). To characterise the properties of tape casting slurries with different temperatures, the rheological measurements were conducted at 20 °C, 21 °C, 25 °C, and 26 °C and fresh slurries were loaded for each experiment to ensure the accuracy of the measurement.

2.2. Data acquisition

In order to eliminate variations related to slurry quality, all green tapes were produced using the same slurry batch according to the consistent procedure on a micro tape-casting machine (KAROcast 300–7, KMS Automation GmbH, Germany). The tape-casting data were collected from both an automated logging system of the casting machine through ELN and physical measurements. Specifically, 29 green tapes (300 cm length and 15 cm width) were performed with different

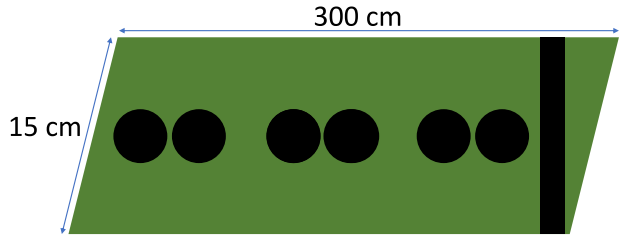

Fig. 3. Circular samples and a stripe were punched from each tape with dimensions 300 cm × 15 cm (length × width).

manufacturing parameters, namely temperatures (between 22 and 60 °C), doctor blade gaps (200, 300, 400 and 500 µm), casting speeds (2.5, 5, and 7.5 mm/s), humidity (recorded in %) and exhaust air volume flow rate (automatically regulated in m^3/h by the machine based upon supply and exhaust fan speeds). Nevertheless, it is worth mentioning that owing to the limitation in control and tracking, humidity was manually recorded once both inside and outside the machine at the time of casting implementation using a hygrometer of the tape-casting device. After the tape-casting step, at least six circular samples with a diameter of 43.85 mm and one stripe sample were punched from each tape (Fig. 3). The stripe sample was used to evaluate the homogeneity of the green tape's thickness distribution. For each circular green sample, at least nine thickness values were measured, and the respective green density was then calculated from the weight-to-volume ratio. Subsequently, the green samples were labelled with their corresponding tape ID numbers to track their evolution throughout subsequent processes and subjected to pre-sintering at 1230 °C for 3 h to remove the binder and prepare for the subsequent sintering step. Following pre-sintering, the samples were sintered at 1400 °C for 5 h, yielding sintered samples with the desired microstructure and porosity. This second sintering step mimics the co-sintering of the electrolyte together with the fuel electrode and the support in the typical SOC half-cell manufacturing sequence. Thereafter, the thickness and density of sintered samples were determined experimentally. Finally, a reduction step was carried out in an Ar/H_2 atmosphere at 900 °C for 3 h to achieve metallic Ni as for the final functional properties, followed by the experimental determination of the reduced samples' thickness and density. More information about thermal treatment can be found in the Supporting Information.

2.3. Correlation analysis

Correlation analysis techniques have been employed to analyse the fundamental correlation, relationships and characteristics between key manufacturing parameters and the green tape properties within the dataset. The most prevalent techniques are Pearson's correlation coefficient and Spearman's correlation coefficient. Pearson's correlation coefficient measures the linearity correlation between two continuous random variables and is given by

$$\rho_p = \frac{\sum_{i=1}^{n}\left(x_i-\bar{x}\right)\left(y_i-\bar{y}\right)}{\sqrt{\sum_{i=1}^{n}\left(x_i-\bar{x}\right)^2\sum_{i=1}^{n}\left(y_i-\bar{y}\right)^2}}, \tag{1}$$

where n is sample size, x_i and y_i are the values of variables X and Y for the ith observation, and $\bar{x}$ and $\bar{y}$ are the means of variables X and Y, respectively [53].

Spearman's correlation coefficient is utilised to capture monotonic relationship between two continuous random variables and is defined as

$$\rho_s = 1 - \frac{6\sum_{i=1}^{n} d_i^2}{n\left(n^2-1\right)}, \tag{2}$$

where d_i denotes the difference between the ranks of x_i and y_i for the ith observation [53].

2.4. Machine learning modelling

The full dataset comprises 357 observations. Each sample is described by 5 distinct attributes, such as temperature, doctor blade gap, casting speed, humidity, and exhaust air volume flow rate, used as inputs to train independent ML models so as to predict the green thickness as well as green density for the tape-casting process. The green thickness and green density are then used as inputs for the sintering models to predict the thickness and density of the sintered tape. Similarly, the reduction stage models utilised sintered thickness and sintered density to forecast thickness and density in the reduced state. Furthermore, to track the tape's evolution as well as capture batch-specific variations of the tape after the tape-casting process, the tape ID numbers were also considered as an important feature in enhancing the performance of ML models in the sintering and reduction process.

In preparation for modelling, the raw dataset is randomly divided into an 80% training set and a 20% testing set. The training set is used to train models to make predictions, while the testing set is used to evaluate the performance of trained models on unseen data. Indeed, the testing dataset includes experimental data that models have not seen during the training yet, equivalent to testing the models against previously unperformed experiments. The modular ML approach was adopted to model a series of multi-stage manufacturing processes of the fuel electrode support from tape casting to sintering and to reduction, which enables the optimisation of the prediction for the physical properties of the tape at each fabrication stage. For each manufacturing process, a number of regression algorithms were evaluated for each prediction task. Repeated k-Fold Cross-Validation, with k = 10 and 3 repetitions, was performed for model selection and hyperparameter tuning to prevent overfitting. Specifically, the training set was randomly split into 10 equal folds. In each iteration of a 10-fold process, the model was trained using 9 folds and then validated on the remaining fold. This procedure was repeated 10 times, where each fold served as the validation fold once. Subsequently, the entire 10-Fold Cross-Validation procedure was reiterated 3 times with different randomisations each time, which resulted in the production of 30 distinct performance evaluations in total. The scores from all repetitions are finally averaged to obtain the final score for model assessment. Mean Squared Error (MSE) was used as a primary loss function for the optimisation during this cross-validation process, and MSE is defined as

$$\mathrm{MSE} = \frac{1}{n}\sum_{i=1}^{n}\left(y_i-\hat{y}_i\right)^2, \tag{3}$$

where n is the number of observations, y_i represents the ith observed value, and $\hat{y}_i$ is the ith predicted value.

The algorithm with the optimal set of hyperparameters demonstrating the best performance on this cross-validation phase would be selected as the final model for each specific prediction task. The final models were then re-trained on the entire training dataset and evaluated on the testing dataset using key regression metrics, namely mean absolute error (MAE), root mean squared error (RMSE), and coefficient of determination (R^2). These are defined as follows:

$$\mathrm{MAE} = \frac{1}{n}\sum_{i=1}^{n}\left|y_i-\hat{y}_i\right|, \tag{4}$$

$$\mathrm{RMSE} = \sqrt{\mathrm{MSE}} = \sqrt{\frac{\sum_{i=1}^{n}\left(y_i-\hat{y}_i\right)^2}{n}}, \tag{5}$$

and

$$R^2 = 1 - \frac{\sum_{i=1}^{n}\left(y_i-\hat{y}_i\right)^2}{\sum_{i=1}^{n}\left(y_i-\bar{y}\right)^2}, \tag{6}$$

where $\bar{y}$ is the mean of the observed value.

3. Results and discussion

3.1. Rheological characterisation

During the tape-casting process, the slurry is subjected to a shear rate. This shear rate can be approximated as the ratio of the casting speed to the doctor blade gap [54]. Thus, for non-newtonian fluids such as casting slurries used in this study, the viscosity changes resulting from the changes in the shear rates or doctor blade gaps will alter the fluid mechanical conditions during tape casting, eventually affecting the thickness and uniformity of the green tape. The rheological characterisation of the slurry is shown in Fig. 4, illustrating the dependence of viscosity upon shear rate at four different temperatures: 20, 21, 25, and 26 °C. The shear-rate range corresponds to the actual experiment when we performed the tape casting. These viscosity curves give information about the shear-rate range used for our experiments throughout the tape-casting process. In general, the viscosity decreases as the shear rate increases, indicating that the slurry exhibits shear-thinning, also known as pseudoplasticity, behaviour [55,56]. Furthermore, Fig. 4 also highlights that temperature has an impact on the viscosity of the slurry. Specifically, the viscosity of the casting slurry decreases as the temperature increases. For instance, at the fixed shear rate, the viscosity at 20 °C is higher than that of 21, 25 and 26 °C (Fig. 4). Since the viscosity reflects the flow behaviour of the slurry, these understandings are critical for controlling the flow characteristics of the slurry, which directly impacts the tape casting process and the quality of the resulting green tape.

3.2. Exploratory data analysis

3.2.1. Tape casting

A combination of Pearson and Spearman correlation methods is commonly used to detect both types of relationships that might not be captured through a single method, enabling us to gain a more comprehensive understanding of the correlations between process parameters and the physical properties of the green tape. Fig. 5 shows the Pearson and Spearman correlation coefficient between the process parameters and the output properties of the green tape, revealing physical meaningful trends. In general, both correlation methods are consistent for all pairs except for pairs of volume flow rate and the

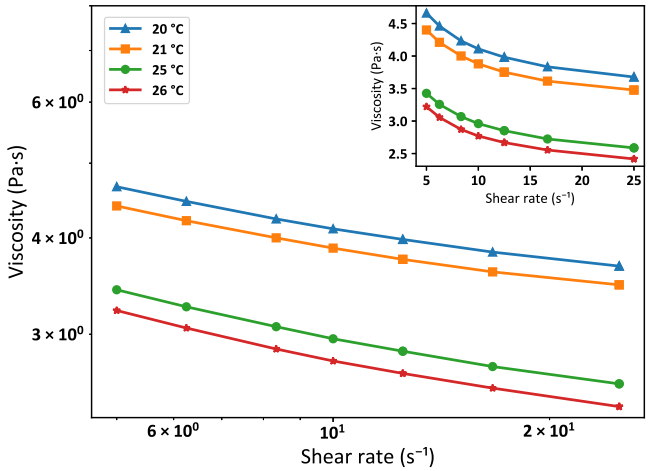

Fig. 4. Viscosity curves of the slurry at varied temperatures: 20 °C, 21 °C, 25 °C, and 26 °C. All measurements were concentrated on the shear-rate range corresponding to our experiments during the tape-casting process. The main plot shows the viscosity curves on a double logarithmic scale, while the inset displays the curves on a linear scale.

outputs. Specifically, the correlation heatmap shows strong positive correlations between the doctor blade gap and the green thickness in terms of Pearson correlation ($\rho_p = 0.96$) and Spearman correlation ($\rho_s = 0.90$), indicating that the doctor blade gap directly controls the tape thickness with a near-linear physical relationship. This confirms the fundamental physical principle where the higher doctor blade gap leads to the thicker green tape [57,58]. The impact of the doctor blade gap on the green density is much weaker than the impact on the green thickness. Casting speeds exhibit a weak influence on green thickness ($\rho_p = -0.25$ and $\rho_s = -0.26$) and a negligible impact on green density ($\rho_p = 0.11$ and $\rho_s = 0.12$). This indicates that faster casting speed predominantly results in thinner tape [59,60]. Similar to casting speed, temperatures show negative correlations with green thickness ($\rho_p = -0.32$ and $\rho_s = -0.44$) and positive correlations with green density ($\rho_p = 0.50$ and $\rho_s = 0.48$). Nevertheless, the impact of the temperature on the physical properties of the green tape is stronger than the casting speeds, indicating the importance of the temperature in producing the green tape using our tape-casting device. Additionally, humidity shows positive correlations with green thickness ($\rho_p = 0.44$ and $\rho_s = 0.54$), illustrating a nonlinear relationship. In contrast, the correlation heatmap shows that humidity is a factor in decreasing the green density of the green tape. The inconsistent correlation for exhaust air volume flow rate between Pearson and Spearman correlation coefficient implies that the impact of this factor is not straightforward and difficult to capture using standard correlation analysis. This complexity may result from its dependence upon the impact of other manufacturing conditions, particularly temperature and humidity. Indeed, the temperature, humidity, and exhaust air volume flow rate are frequently interconnected within the tape-casting process (Figure S1). Therefore, changes in temperature or humidity may result in fluctuations in the exhaust air volume flow rate inside the tape-casting machine. The correlation heatmaps amongst process parameters, along with scatter plots illustrating the relationship between process parameters and green tape properties, are provided in the Supporting Information.

3.2.2. Sintering and reduction

The evolution of the sample properties after the sintering and reduction process was investigated by using scatter plots (Fig. 6). Fig. 6a demonstrates a strong linear correlation between green thickness and sintered thickness, confirming that the green samples with higher thickness lead to the thicker sintered thickness after sintering in the same conditions. Meanwhile, although Fig. 6b displays the increasing trend for the density of the sample after sintering, the scatter plot of green density and sintered density is more scattered. This dispersion explains differences in initial green density as well as complex material transformations throughout the sintering process.

During the reduction process, the thickness change is quite minimal, and a strong linear relationship is also observed in thickness transitions between the sintering and reduction stages (Fig. 6c). Fig. 6d indicates that the density after reduction is slightly lower than the sintered density due to the reduction of NiO to Ni, and the sintered samples with higher density will retain the higher density in the reduced state. These results are physically expected and show that the sintering quality is crucial for the final microstructure.

Table 2
Performance of optimised machine learning models for SOC support fabrication stages on the independent testing set. All models showed strong predictive accuracy, with R^2 scores consistently exceeding 0.9 for all tasks, indicating that the majority of the variance in unseen data could be explained. The MAE and RMSE values are expressed in the unit of each output (e.g., thickness in μm, density in g/cm^3). Thus, these errors are relatively small compared to their actual measurement scales.

Process stage	Predicted output	Optimal algorithm	R^2	MAE	RMSE
Tape Casting	Green Thickness	Extra Trees	0.99	1.327	1.780
	Green Density	Extra Trees	0.91	0.012	0.015
Sintering	Sintered Thickness	Extra Trees	0.99	0.397	0.588
	Sintered Density	Extra Trees	0.98	0.013	0.021
Reduction	Reduced Thickness	Ridge regression	0.99	0.237	0.306
	Reduced Density	Ridge regression	0.99	0.006	0.008

3.3. Machine learning performance

Several regressors were explored and evaluated to predict the thickness and density for each manufacturing stage, namely Ridge Regression, Support Vector Regression, Random Forest, Extra Trees, and Gradient Boosting. Amongst them, the Extra Trees regressor exhibits robust predictive performance for both green thickness and green density with R^2 scores of 0.99 and 0.91, respectively. This explains the nature of the dataset. In fact, the correlation assessment results suggest that the tape-casting dataset exhibits both multicollinearity and non-linear relationships between process parameters and green tape properties. Tree-based models are particularly well-suited for this type of data, as they can capture complex non-linear patterns and remain robust in the presence of multicollinearity [61]. Moreover, these models are less sensitive to non-normal feature distributions and do not require feature scaling [62,63], which is advantageous when working with raw experimental datasets. This explains why tree-based algorithms such as Extra Trees demonstrated strong predictive performance in modelling the tape-casting process.

In the sintering and reduction stages, the Extra Trees Regressor remained the best-performing model for predicting sintered thickness and density with R^2 scores of 0.99 and 0.98, respectively. This is mainly due to the complexity of material behaviour throughout heat treatment. Nonetheless, Ridge Regression with L2 regularisation demonstrated excellent performance, achieving an R^2 score of 0.99 in predicting thickness and density in the reduced state. In fact, the reduction stage mainly involves the reduction of NiO to Ni, resulting in only minor changes in thickness and density. Therefore, the thickness and density after reduction exhibit near-linear dependencies on the sintered thickness and density. Consequently, this explains why Ridge Regression, a linear model with regularisation, was most appropriate to our dataset in the case of the reduction stage. Fig. 7 illustrates regression plots comparing the target values to the predicted values to assess the accuracy of developed ML models for each prediction task. It can be observed that most of the predicted values align well with the target data points, indicating high prediction accuracy of the models. The

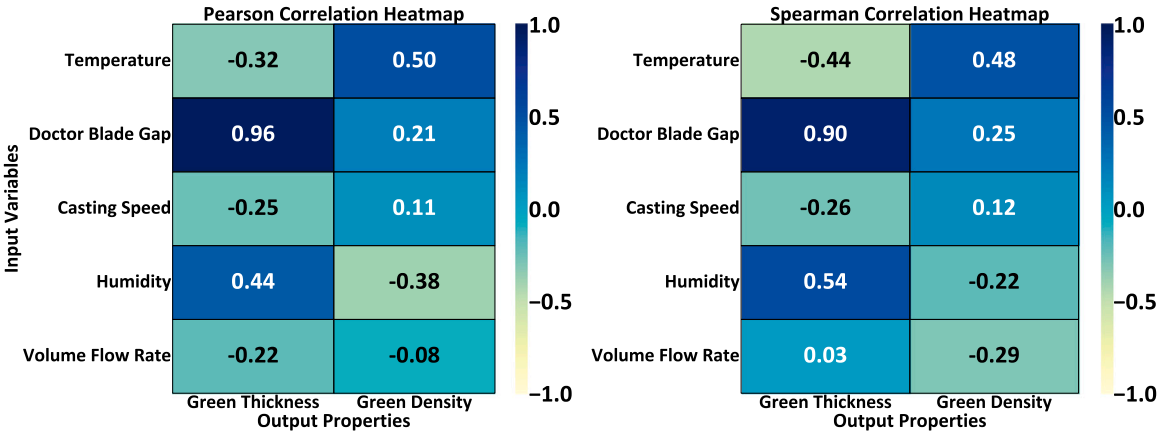

(a) *Pearson method* (b) *Spearman method*

Fig. 5. Correlation heatmap between key manufacturing parameters and the relevant outputs for the tape-casting process, ranging from −1 (perfect negative correlation) to 1 (perfect positive correlation), where 0 implies no correlation: (a) Pearson correlation heatmap between manufacturing parameters and the physical properties of the green tape, and (b) Spearman correlation heatmap between manufacturing parameters and the physical properties of the green tape.

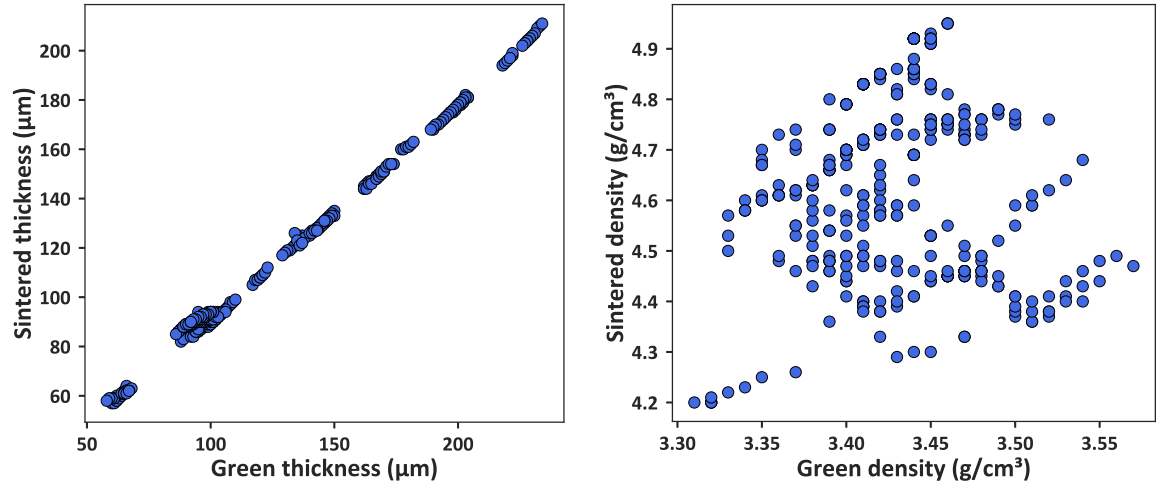

(a) *Green thickness vs sintered thickness* (b) *Green density vs sintered density*

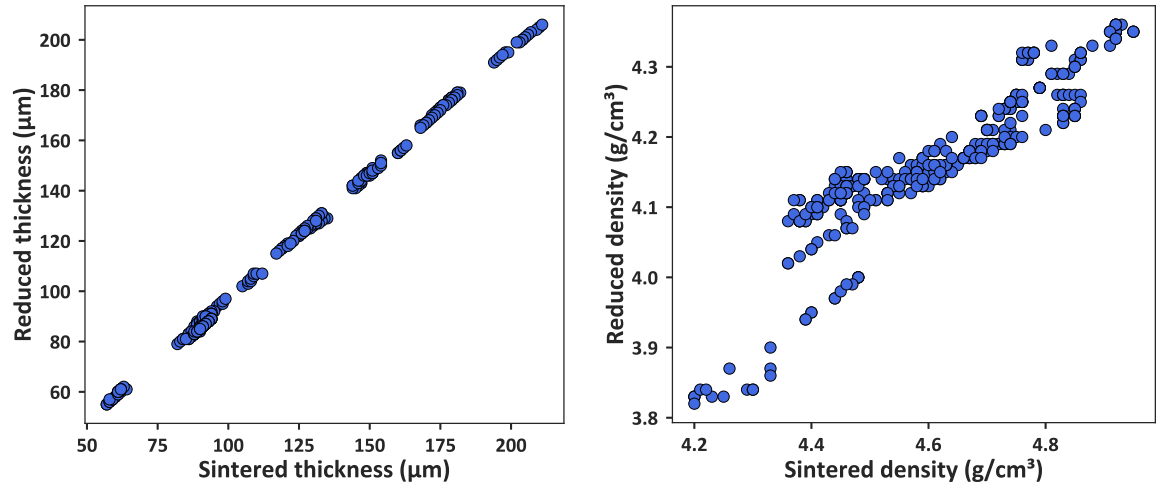

(c) *Sintered thickness vs reduced thickness* (d) *Sintered density vs reduced density*

Fig. 6. Scatter plots representing the relationship of tape properties after sintering and reduction process: (a) Green thickness and sintered thickness, (b) Green density and sintered density, (c) Sintered thickness and reduced thickness, and (d) Sintered density and reduced density.

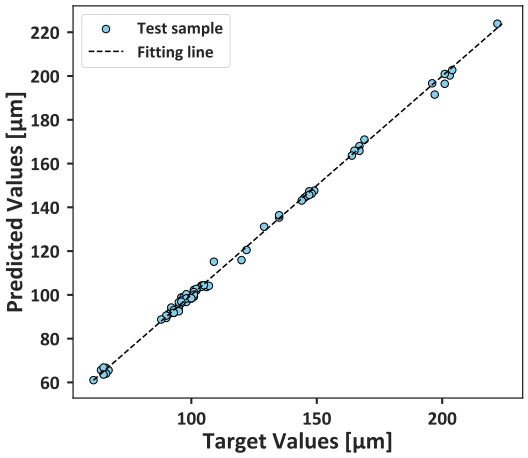

(a) *Green Thickness*

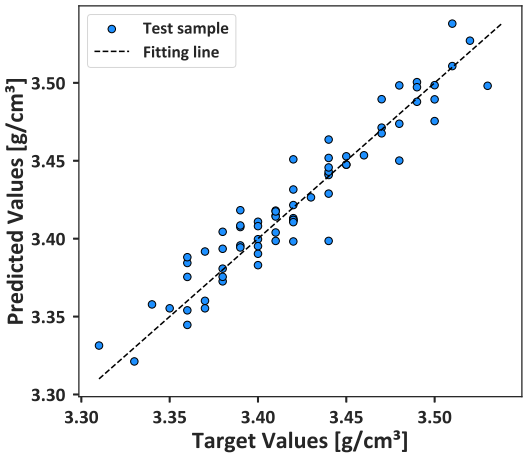

(b) *Green Density*

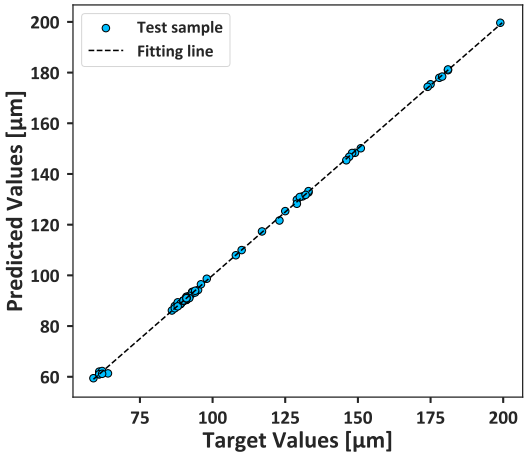

(c) *Sintered Thickness*

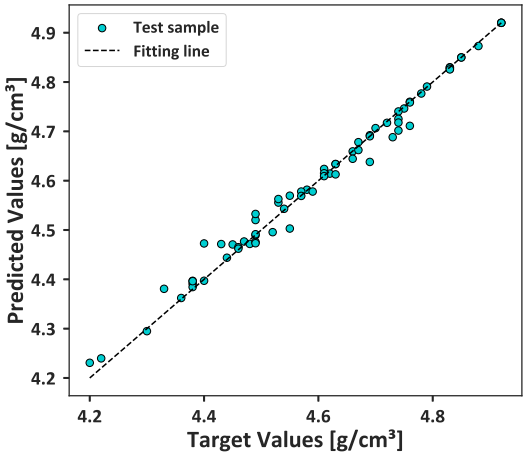

(d) *Sintered Density*

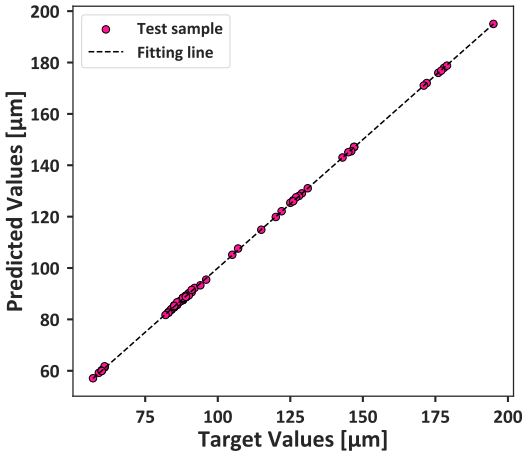

(e) *Reduced Thickness*

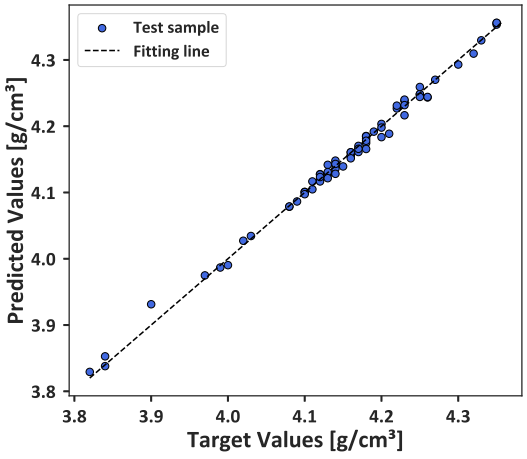

(f) *Reduced Density*

Fig. 7. Comparison plots of predicted values against target values for physical properties of the tape at different manufacturing stages: (a) Green thickness, (b) Green density, (c) Sintered thickness, (d) Sintered density, (e) Reduced thickness, and (f) Reduced density.

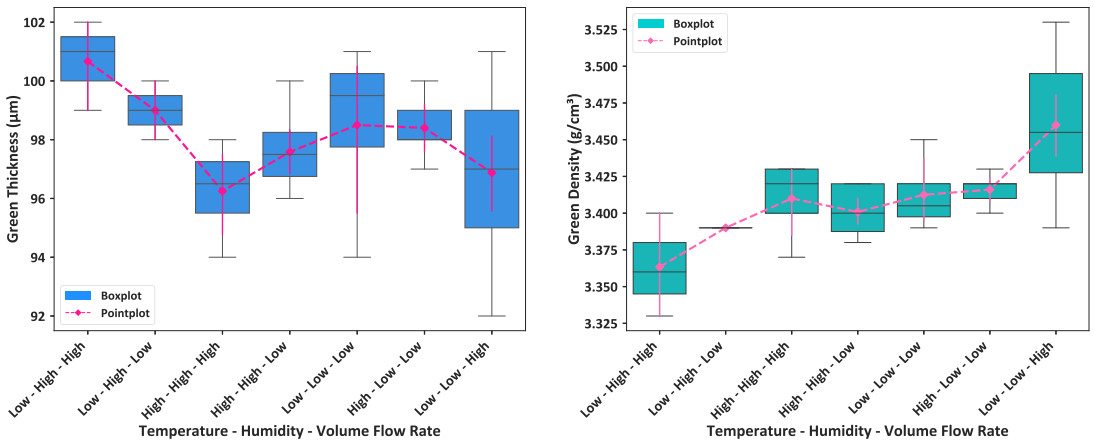

(a) *Green Thickness* (b) *Green Density*

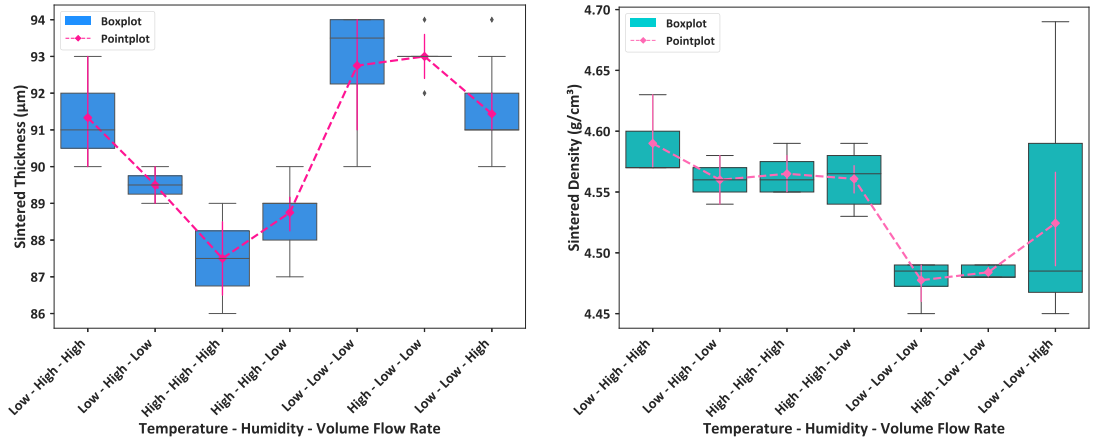

(c) *Sintered Thickness* (d) *Sintered Density*

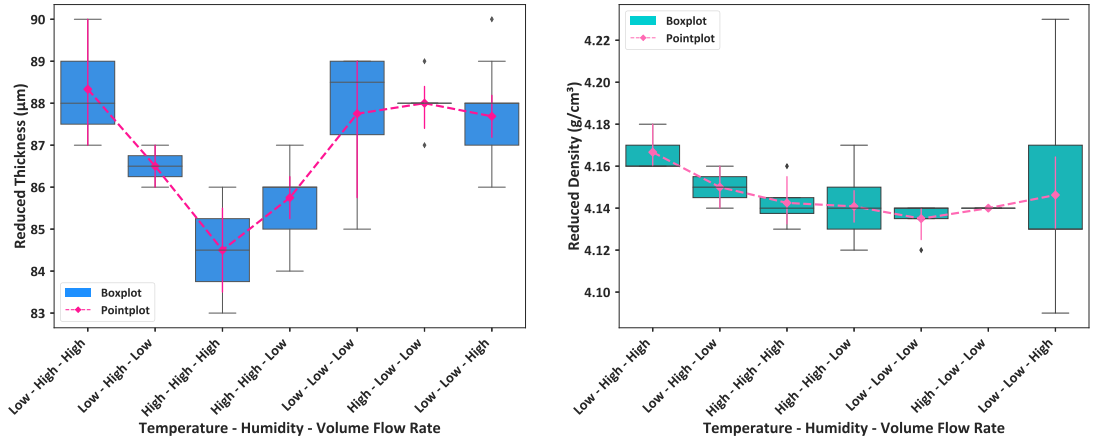

(e) *Reduced Thickness* (f) *Reduced Density*

Fig. 8. Analysis plots demonstrating the impact of three-manufacturing-parameter combinations (e.g. temperature, humidity and exhaust air volume flow rate) on (a) Green thickness, (b) Green density, (c) Sintered thickness, (d) Sintered density, (e) Reduced thickness, and (f) Reduced density. The boxplots compare various condition groups. Point plots represent the mean value and the tendency, accompanied by its 95% confidence interval. All analyses were implemented for the tapes produced using the same doctor blade of 300 µm and the casting speed of 5 mm/s. The investigated temperature, humidity and volume flow rate in the exhaust air varied in the ranges of 22.4–33.9 °C, 29%–50%, and 69.05–74.48 m^3/h, respectively. "Low" and "High" levels correspond to values below and above the median (50th percentile) of each parameter, respectively.

performance of the optimised ML models for each stage of the SOC support manufacturing process is summarised in Table 2. Each row represents a specific prediction task with respect to the corresponding stage, detailing the selected optimal algorithm and its performance metrics on the independent testing set.

3.4. Impact of manufacturing parameters on material physical properties

As already mentioned above, in addition to the known influences of the doctor blade gap and casting speed, condition parameters such as temperature, humidity, and exhaust air volume flow rate also have

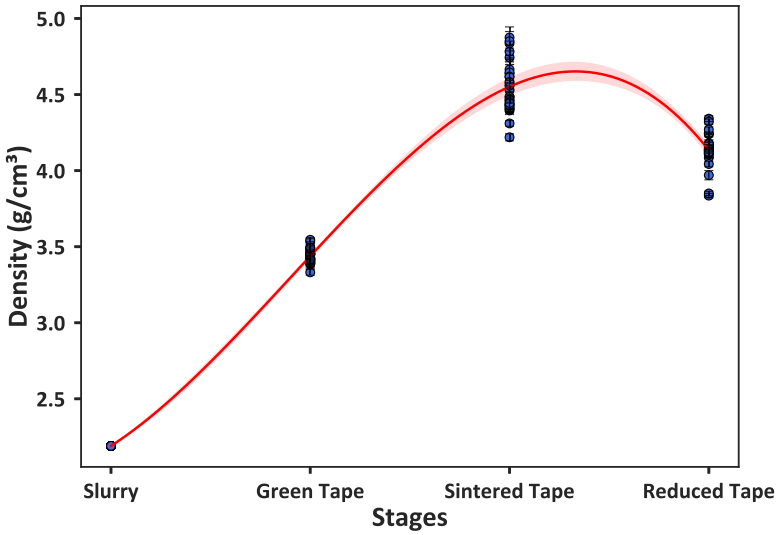

Fig. 9. Density evolution during fuel-electrode support manufacturing stages from slurry to green, sintered, and reduced tapes. Each data point represents the average density of an individual tape. Error bars indicate the corresponding standard deviation of the intra-tape.

crucial roles to play in determining the final properties of the green tape in our study. These factors often exert simultaneous effects on the tape rather than acting in isolation. To further analyse the combined impacts of these three parameters on the tape properties, we analyse the tapes produced using a consistent doctor blade gap of 300 μm, a casting speed of 5 mm/s, the same supply and exhaust fan speeds, and a consistent initial temperature setting on the tape casting machine. Since these tapes were fabricated at different times, the humidity levels varied with each experiment. This ensures the reliability of comparisons and analysis regarding the subtle, yet often hard-to-detect, influence of humidity.

Fig. 8 illustrates the influence of three manufacturing parameters on the tape properties across three manufacturing stages: tape casting, sintering, and reduction process. The data are visualised using boxplots alongside point plots, providing comprehensive insights about data distribution and central tendency for each condition group. Specifically, in the tape-casting stage, both thickness and density demonstrate variations according to temperature, humidity, and exhaust air volume flow rate. The "Low-High-High" condition yields the highest mean green thickness, while the "High-High-High" condition results in the lowest mean thickness. Conversely, green density generally increases across the conditions, with the "Low-Low-High" condition exhibiting the highest mean green density. Figs. 8a and 8b offer valuable insights for optimising the tape casting process. For instance, if the goal is to produce tapes with higher green thickness, the "Low-High-High" condition may be preferred, despite the resultant lower green density. Conversely, for achieving the higher density, the "Low-Low-High" condition represents a suitable option. Meanwhile, to attain a balance of relatively higher mean values and less variability for both green thickness and density, we could consider to control the condition to "High-High-High", "High-High-Low", and "High-Low-Low".

In the sintering and reduction stages, initial manufacturing conditions indirectly affected the properties of the sintered and reduced tapes through tape casting. This indirect effect suggests a strong retention of characteristics from the green tape stage into subsequent processing. Analysis of Figs. 8c and 8e confirms that tape thickness consistently decreased across all experimental groups after both the sintering and reduction processes. Notably, the change in thickness between sintered and reduced tapes was minor when compared to the more significant thickness transformation observed between the green and sintered tapes. Furthermore, Figs. 8d and 8f illustrate a substantial increase in tape density following the sintering process, while a slight decrease in density was observed after the reduction stage. By comprehensively analysing tape properties, including thickness and density, across all three stages (green, sintered, and reduced tape) in relation to temperature, humidity, and volume flow rate, the results indicate that the "High-High-Low" condition consistently yields higher values and lower variability for both thickness and density. Nevertheless, if the primary objective is to achieve tapes with exceptionally high thickness and density, irrespective of their variability, the "Low-Low-High" condition merits consideration.

3.5. Density evolution during fuel electrode support fabrication

Fig. 9 illustrates the evolution of the average density across various stages: slurry, green tape, sintered tape and reduced tape. Despite differences amongst the individual tape samples, a consistent trend was observed across all cases. Therefore, a single regression curve was fitted to represent the overall behaviour. Overall, it is obvious that the density underwent significant changes during fabrication. Specifically, the density was lowest at around 2.19 g/cm^3 in the slurry stage. After tape casting and drying, the density achieved a value within a range of 3.33 and 3.55 g/cm^3 depending upon the manufacturing conditions and parameters in our study. This results from the solvents evaporating and the material particles undergoing closer packing. During the sintering at 1400 °C, the binder and organic additives were completely burned off, while particles fused into a solid coherent mass. As a result, the tape experiences a significant increase in density, reaching values in the range of 4.22 and 4.87 g/cm^3. Finally, the reduction of NiO to Ni results in a slight decrease in density caused by oxygen loss, with the final density ranging from 3.84 to 4.34 g/cm^3. The figure provides a clear visualisation of the physical transitions in density throughout the manufacturing stages, highlighting the consistency of the process.

4. Conclusions and perspectives

We presented a data-driven machine learning framework to predict the thickness and density of the fuel electrode support across various fabrication processes, namely tape casting, sintering, and reduction processes. Viscosity measurements at various temperatures were employed to investigate the impact of temperature on the rheological properties of the slurry. Our dataset was collected experimentally from the automated logging system of our tape casting machine via ELN and physical measurements, enabling ML to be applied to ceramics tape casting for the first time. We analyse the experimental data to detect the relationship between the manufacturing conditions and physical

properties of the green tape, especially the direct impact of temperature, humidity and exhaust air volume flow rate on green thickness and green density, which indirectly affects the thickness and density of the sintered and reduced tape. Therefore, it is worth noting that the tape casting process could be optimised if humidity and exhaust air volume flow rate inside the machine can be tracked and controlled.

Despite this present work using one optimised slurry formulation, our workflow framework can be extended by incorporating not only varying slurry compositions but also different conditions during thermal treatment processes. This enables a more comprehensive analysis of the relationship between manufacturing parameters and physical properties of the tape at each manufacturing stage.

The reported work further indicates that the thickness and density of the fuel-electrode support for each manufacturing process can be predicted with high accuracy by using ML models trained on high-quality data from the experiment. Although our current study utilised semi-automated data collection, which included extracting log files from the tape casting machine and manually measuring sample properties, the developed ML models still exhibited strong predictive performance. Nevertheless, the overall accuracy of ML models can be further enhanced, provided that a comprehensive automated data acquisition process is implemented to reduce potential human error in practice. Developing the automated data acquisition pipeline coupled to an ML framework will not only enhance the predictive performance but also allow the development of models to optimise the manufacturing process.

In the era of smart manufacturing, a promising direction for future research lies in the integration of data-driven ML approaches into the manufacturing pipeline of fuel-electrode supports as well as other components of SOCs, taking inspiration from the concept of digital twin already elaborated in the context of battery manufacturing [64,65]. As a first step toward automation, we have successfully integrated ELN, specifically eLabFTW, into our tape casting system to automatically collect process data. To fully realise the benefits of ML integration, it is essential to establish a fully automated infrastructure for acquiring high-quality, diverse data from each stage of the manufacturing process. Moving forward, physical measurements should also be automated and ideally conducted using non-contact methods to improve both measurement precision and accuracy, thereby enhancing the overall data quality. Coupling automated data acquisition with ML offers significant potential for predicting material properties, and thus enables better decision-making throughout the manufacturing workflow [66]. Such an end-to-end automated pipeline would minimise human-induced error and enable large-scale collection of high-quality data with diverse input parameters. This provides a solid foundation for training robust ML models capable of optimising the fabrication process of SOC component layers more intelligently and efficiently.

CRediT authorship contribution statement

Tan Le-Dinh: Writing – original draft, Visualization, Validation, Software, Methodology, Investigation, Formal analysis, Data curation, Conceptualization. **Hartmut Schlenz:** Writing – review & editing, Validation, Supervision, Methodology, Conceptualization. **Norbert H. Menzler:** Writing – review & editing, Supervision. **Alejandro A. Franco:** Writing – review & editing, Supervision, Project administration, Funding acquisition, Conceptualization. **Olivier Guillon:** Writing – review & editing, Supervision, Project administration, Funding acquisition.

Declaration of competing interest

The authors declare that they have no known competing financial interests or personal relationships that could have appeared to influence the work reported in this paper.

Acknowledgements

T.L.D and A.A.F acknowledge the Region Hauts-de-France and Université de Picardie Jules Verne for the funding support. T.L.D, H.S., N.H.M., and O.G. acknowledge Forschungzentrum Jülich GmbH for the support. T.L.D., H.S., N.H.M., O.G. and A.A.F. gratefully acknowledge funding by Federal Ministry of Economic Affairs and Energy of Germany (Bundesministerium für Wirtschaft und Energie der Bundesrepublik Deutschland, Project-No.: 03EI3085A, ML4SOC). A.A.F. acknowledges the Institut Universitaire de France for the support. The authors acknowledge Ralf Kauert and Eugen Susakin for the preparation of the slurry and the green tape used for the extraction of the experimental data used in this work. The authors acknowledge Denise Ramler for assistance with slurry viscosity measurements.

Data availability

Data will be made available on request.

References

[1] Guan D, Wang B, Zhang J, Shi R, Jiao K, Li L, Wang Y, Xie B, Zhang Q, Yu J, Zhu Y, Shao Z, Ni M. Hydrogen society: from present to future. Energy Env Sci 2023;16:4926–43. http://dx.doi.org/10.1039/D3EE02695G.

[2] Shen Z, Bassat JM, Fourcade S, Demourgues A, Durand E, Teule-Gay L, Duttine M, Gamon J. Is fluorine incorporation in the $La_{0.6}Sr_{0.4}Co_{0.2}Fe_{0.8}O_{3-\delta}$ improving its electrochemical behavior for solid oxide cells applications? Adv Energy Mater 2024;14:2401518. http://dx.doi.org/10.1002/AENM.202401518.

[3] Tariq U, Khan MZ, Gohar O, Babar ZUD, Ali F, Malik RA, Starostina IA, Samia, Rehman J, Hussain I, Saleem M, Ghaffar A, Marwat MA, Zheng K, Motola M, Hanif MB. Bridging the gap between fundamentals and efficient devices: Advances in proton-conducting oxides for low-temperature solid oxide fuel cells. J Power Sources 2024;613:234910. http://dx.doi.org/10.1016/J.JPOWSOUR.2024.234910.

[4] Khan MZ, Iltaf A, Ishfaq HA, Khan FN, Tanveer WH, Song R-H, Mehran MT, Saleem M, Hussain A, and ZM. Flat-tubular solid oxide fuel cells and stacks: a review. J Asian Ceram Soc 2021;9(3):745–70. http://dx.doi.org/10.1080/21870764.2021.1920135.

[5] Xiao M, Liu Z, Di H, Bai Y, Yang G, Medvedev DA, Luo Z, Wang W, Zhou W, Ran R, Shao Z. High-entropy materials for solid oxide cells: Synthesis, applications, and prospects. J Energy Chem 2025;104:268–96. http://dx.doi.org/10.1016/J.JECHEM.2024.12.009.

[6] Menzler N, Tietz F, Uhlenbruck S, Buchkremer H, Stöver D. Materials and manufacturing technologies for solid oxide fuel cells. J Mater Sci 2010;45:3109–35. http://dx.doi.org/10.1007/s10853-010-4279-9.

[7] Blum L, Buchkremer H-P, Gross S, Gubner A, de Haart LGJB, Nabielek H, Quadakkers WJ, Reisgen U, Smith MJ, Steinberger-Wilckens R, Steinbrech RW, Tietz F, Vinke IC. Solid oxide fuel cell development at Forschungszentrum Juelich. Fuel Cells 2007;7(3):204–10. http://dx.doi.org/10.1002/fuce.200600039.

[8] Lenser C, Udomsilp D, Menzler NH, Holtappels P, Fujisaki T, Kwati L, Matsumoto H, Sabato AG, Smeacetto F, Chrysanthou A, Molin S. 9 - solid oxide fuel and electrolysis cells. In: Guillon O, editor. Advanced ceramics for energy conversion and storage. Elsevier series on advanced ceramic materials, Elsevier; 2020, p. 387–547. http://dx.doi.org/10.1016/B978-0-08-102726-4.00009-0.

[9] Sarner S, Schreiber A, Menzler NH, Guillon O. Recycling strategies for solid oxide cells. Adv Energy Mater 2022;12(35):2201805. http://dx.doi.org/10.1002/aenm.202201805.

[10] Nguyen QM, Takahashi T. Science and technology of ceramic fuel cells. Elsevier Science; 1995, p. 366.

[11] Fu C, Chan SH, Liu Q, Ge X, Pasciak G. Fabrication and evaluation of Ni-GDC composite anode prepared by aqueous-based tape casting method for low-temperature solid oxide fuel cell. Int J Hydrog Energy 2010;35:301–7. http://dx.doi.org/10.1016/J.IJHYDENE.2009.09.101.

[12] Timurkutluk B, Mat MD. Effects of anode fabrication parameters on the performance and redox behavior of solid oxide fuel cells. J Power Sources 2014;258. http://dx.doi.org/10.1016/j.jpowsour.2014.02.023.

[13] Richard E. Mistler ERT. Tape casting: Theory and practice. The American Ceramic Society, Westerville, OH; 2000.

[14] Hubadillah SK, Othman MHD, Matsuura T, Ismail AF, Rahman MA, Harun Z, Jaafar J, Nomura M. Fabrications and applications of low cost ceramic membrane from kaolin: A comprehensive review. Ceram Int 2018;44:4538–60. http://dx.doi.org/10.1016/J.CERAMINT.2017.12.215.

[15] Naebe M, Shirvanimoghaddam K. Functionally graded materials: A review of fabrication and properties. Appl Mater Today 2016;5:223–45. http://dx.doi.org/10.1016/J.APMT.2016.10.001.
[16] Letilly M, Joubert O, Caldes MT, Salle ALGL. Tape casting fabrication, co-sintering and optimisation of anode/electrolyte assemblies for SOFC based on BIT07-Ni/BIT07. Int J Hydrog Energy 2012;37:4346–55. http://dx.doi.org/10.1016/J.IJHYDENE.2011.11.140.
[17] Smay JE, Lewis JA. Structural and property evolution of aqueous-based lead zirconate titanate tape-cast layers. J Am Ceram Soc 2001;84(11):2495–500. http://dx.doi.org/10.1111/j.1151-2916.2001.tb01042.x.
[18] Leng YJ, Chan SH, Khor KA, Jiang SP. Performance evaluation of anode-supported solid oxide fuel cells with thin film YSZ electrolyte. Int J Hydrog Energy 2004;29:1025–33. http://dx.doi.org/10.1016/J.IJHYDENE.2004.01.009.
[19] Kim JH, Ko H, Yeo DH, Park Z, Kumar U, Yoo KH, Nasridinov A, Cho SB. A versatile strategy for hybridizing small experimental and large simulation data: A case for ceramic tape-casting process. Mater Des 2023;234. http://dx.doi.org/10.1016/j.matdes.2023.112357.
[20] Jabbari M, Bulatova R, Tok AI, Bahl CR, Mitsoulis E, Hattel JH. Ceramic tape casting: A review of current methods and trends with emphasis on rheological behaviour and flow analysis. Mater Sci Eng: B 2016;212:39–61. http://dx.doi.org/10.1016/J.MSEB.2016.07.011.
[21] Gardini D, Deluca M, Nagliati M, Galassi C. Flow properties of PLZTN aqueous suspensions for tape casting. Ceram Int 2010;36:1687–96. http://dx.doi.org/10.1016/J.CERAMINT.2010.03.011.
[22] Tok AI, Boey FY, Khor KA. Tape casting of high dielectric ceramic composite substrates for microelectronics application. J Mater Process Technol 1999;89–90:508–12. http://dx.doi.org/10.1016/S0924-0136(99)00131-4.
[23] Tok A, Boey F, Khor K. Tape casting of high dielectric ceramic substrates for microelectronics packaging. J Mater Eng Perform 1999;8:469–72. http://dx.doi.org/10.1361/105994999770346783.
[24] Yang K, Liu J, Wang Y, Shi X, Wang J, Lu Q, Ciucci F, Yang Z. Machine-learning-assisted prediction of long-term performance degradation on solid oxide fuel cell cathodes induced by chromium poisoning. J Mater Chem A 2022;10:23683–90. http://dx.doi.org/10.1039/D2TA03944C.
[25] Sun W, Zheng Y, Yang K, Zhang Q, Shah AA, Wu Z, Sun Y, Feng L, Chen D, Xiao Z, Lu S, Li Y, Sun K. Machine learning-assisted molecular design and efficiency prediction for high-performance organic photovoltaic materials. Sci Adv 2019;5(11):eaay4275. http://dx.doi.org/10.1126/sciadv.aay4275.
[26] Zhong X, Gallagher B, Liu S, Kailkhura B, Hiszpanski A, Han TY-J. Explainable machine learning in materials science. Npj Comput Mater 2022;8(1). http://dx.doi.org/10.1038/s41524-022-00884-7.
[27] Wei J, Chu X, Sun X-Y, Xu K, Deng H-X, Chen J, Wei Z, Lei M. Machine learning in materials science. InfoMat 2019;1(3):338–58. http://dx.doi.org/10.1002/inf2.12028.
[28] Wang AY-T, Murdock RJ, Kauwe SK, Oliynyk AO, Gurlo A, Brgoch J, Persson KA, Sparks TD. Machine learning for materials scientists: An introductory guide toward best practices. Chem Mater 2020;32(12):4954–65. http://dx.doi.org/10.1021/acs.chemmater.0c01907.
[29] Mobarak MH, Mimona MA, Islam MA, Hossain N, Zohura FT, Imtiaz I, Rimon MIH. Scope of machine learning in materials research—A review. Appl Surf Sci Adv 2023;18:100523. http://dx.doi.org/10.1016/J.APSADV.2023.100523.
[30] Friederich P, Häse F, Proppe J, Aspuru-Guzik A. Machine-learned potentials for next-generation matter simulations. Nat Mater 2021 20:6 2021;20:750–61. http://dx.doi.org/10.1038/s41563-020-0777-6.
[31] Nguyen BD, Roder M, Danilewsky A, Steiner J, Wellmann P, Sandfeld S. Automated analysis of X-ray topography of 4H-SiC wafers: Image analysis, numerical computations, and artificial intelligence approaches for locating and characterizing screw dislocations. J Mater Res 2022;38. http://dx.doi.org/10.1557/s43578-022-00880-z.
[32] Fernandez F, Saravanan S, Omongos RL, Troncoso JF, Galvez-Aranda DE, Franco AA. Transfer learning assessment of small datasets relating manufacturing parameters with electrochemical energy cell component properties. Npj Adv Manuf 2025 2:1 2025;2:1–14. http://dx.doi.org/10.1038/s44334-025-00024-1.
[33] Vijay U, Galvez-Aranda DE, Zanotto FM, Le-Dinh T, Alabdali M, Asch M, Franco AA. A hybrid modelling approach coupling physics-based simulation and deep learning for battery electrode manufacturing simulations. Energy Storage Mater 2025;75:103883. http://dx.doi.org/10.1016/J.ENSM.2024.103883.
[34] Galvez-Aranda DE, Dinh TL, Vijay U, Zanotto FM, Franco AA. Time-dependent deep learning manufacturing process model for battery electrode microstructure prediction. Adv Energy Mater 2024;14:2400376. http://dx.doi.org/10.1002/AENM.202400376.
[35] Pilania G, Gubernatis JE, Lookman T. Multi-fidelity machine learning models for accurate bandgap predictions of solids. Comput Mater Sci 2017;129:156–63. http://dx.doi.org/10.1016/J.COMMATSCI.2016.12.004.
[36] Isayev O, Oses C, Toher C, Gossett E, Curtarolo S, Tropsha A. Universal fragment descriptors for predicting properties of inorganic crystals. Nat Commun 2017;8(1). http://dx.doi.org/10.1038/ncomms15679.
[37] Duquesnoy M, Lombardo T, Chouchane M, Primo EN, Franco AA. Data-driven assessment of electrode calendering process by combining experimental results, in silico mesostructures generation and machine learning. J Power Sources 2020;480:229103. http://dx.doi.org/10.1016/J.JPOWSOUR.2020.229103.
[38] Gómez-Bombarelli R, Aguilera-Iparraguirre J, Hirzel TD, Duvenaud D, Maclaurin D, Blood-Forsythe MA, Chae HS, Einzinger M, Ha DG, Wu T, Markopoulos G, Jeon S, Kang H, Miyazaki H, Numata M, Kim S, Huang W, Hong SI, Baldo M, Adams RP, Aspuru-Guzik A. Design of efficient molecular organic light-emitting diodes by a high-throughput virtual screening and experimental approach. Nat Mater 2016 15:10 2016;15:1120–7. http://dx.doi.org/10.1038/nmat4717.
[39] Raccuglia P, Elbert KC, Adler PD, Falk C, Wenny MB, Mollo A, Zeller M, Friedler SA, Schrier J, Norquist AJ. Machine-learning-assisted materials discovery using failed experiments. Nat 2016 533:7601 2016;533:73–6. http://dx.doi.org/10.1038/nature17439.
[40] Szymanski NJ, Rendy B, Fei Y, Kumar RE, He T, Milsted D, McDermott MJ, Gallant M, Cubuk ED, Merchant A, Kim H, Jain A, Bartel CJ, Persson K, Zeng Y, Ceder G. An autonomous laboratory for the accelerated synthesis of novel materials. Nat 2023 624:7990 2023;624:86–91. http://dx.doi.org/10.1038/s41586-023-06734-w.
[41] Schlenz H, Baumann S, Meulenberg WA, Guillon O. The development of new perovskite-type oxygen transport membranes using machine learning. Crystals 2022;12(7). http://dx.doi.org/10.3390/cryst12070947.
[42] Lu S, Zhou Q, Ouyang Y, Guo Y, Li Q, Wang J. Accelerated discovery of stable lead-free hybrid organic-inorganic perovskites via machine learning. Nat Commun 2018;9. http://dx.doi.org/10.1038/s41467-018-05761-w.
[43] Butler KT, Davies DW, Cartwright H, Isayev O, Walsh A. Machine learning for molecular and materials science. Nat 2018 559:7715 2018;559:547–55. http://dx.doi.org/10.1038/s41586-018-0337-2.
[44] Duquesnoy M, Boyano I, Ganborena L, Cereijo P, Ayerbe E, Franco AA. Machine learning-based assessment of the impact of the manufacturing process on battery electrode heterogeneity. Energy AI 2021;5:100090. http://dx.doi.org/10.1016/J.EGYAI.2021.100090.
[45] Malki AE, Asch M, Arcelus O, Shodiev A, Yu J, Franco AA. Machine learning for optimal electrode wettability in lithium ion batteries. J Power Sources Adv 2023;20:100114. http://dx.doi.org/10.1016/J.POWERA.2023.100114.
[46] Malki AE, Ati M, Asch M, Franco AA. A machine learning tool to investigate lithium-ion battery degradation under real automotive conditions. J Power Sources 2025;630:236048. http://dx.doi.org/10.1016/J.JPOWSOUR.2024.236048.
[47] Omongos RL, Galvez-Aranda DE, Fernandez F, Vernes A, Franco AA. Digital correlation analysis and optimization of microporous layer through a machine learning workflow for PEMFC applications. J Power Sources 2025;652:237522. http://dx.doi.org/10.1016/J.JPOWSOUR.2025.237522.
[48] Omongos RL, Galvez-Aranda DE, Zanotto FM, Vernes A, Franco AA. Machine learning-driven optimization of gas diffusion layer microstructure for PEM fuel cells. J Power Sources 2025;625:235583. http://dx.doi.org/10.1016/J.JPOWSOUR.2024.235583.
[49] CARPi N, Minges A, Piel M. eLabFTW: An open source laboratory notebook for research labs. J Open Source Softw 2017;2(12):146. http://dx.doi.org/10.21105/joss.00146.
[50] Parthipan R, Anand M, Christensen HM, Hosking JS, Wischik DJ. Defining error accumulation in ML atmospheric simulators. 2024, URL https://arxiv.org/pdf/2405.14714.
[51] Menik S, Ramaswamy L. Towards modular machine learning solution development: Benefits and trade-offs. 2023, URL https://arxiv.org/pdf/2301.09753.
[52] Schafbauer W, Menzler NH, Buchkremer HP. Tape casting of anode supports for solid oxide fuel cells at Forschungszentrum Jülich. Int J Appl Ceram Technol 2014;11:125–35. http://dx.doi.org/10.1111/J.1744-7402.2012.02839.X.
[53] Hogg RV, McKean JW, Craig AT. Introduction to mathematical statistics. Introduction to mathematical statistics. 6th ed. Upper Saddle River, N.J: Pearson Prentice Hall; 2005.
[54] Lombardo T, Hoock JB, Primo EN, Ngandjong AC, Duquesnoy M, Franco AA. Accelerated optimization methods for force-field parametrization in battery electrode manufacturing modeling. Batter Supercaps 2020;3:721–30. http://dx.doi.org/10.1002/BATT.202000049.
[55] Liu T, Ren C, Zhang Y, Wang Y, Lei L, Chen F. Solvent effects on the morphology and performance of the anode substrates for solid oxide fuel cells. J Power Sources 2017;363. http://dx.doi.org/10.1016/j.jpowsour.2017.07.110.
[56] Tok AI, Boey FY, Lam YC. Non-Newtonian fluid flow model for ceramic tape casting. Mater Sci Eng: A 2000;280. http://dx.doi.org/10.1016/S0921-5093(99)00691-7.
[57] Timurkutluk B, Dokuyucu S. The role of tape thickness on mechanical properties and performance of electrolyte supports in solid oxide fuel cells. Ceram Int 2018;44. http://dx.doi.org/10.1016/j.ceramint.2018.06.205.
[58] Timurkutluk B, Celik S, Ucar E. Influence of doctor blade gap on the properties of tape cast NiO/YSZ anode supports for solid oxide fuel cells. Ceram Int 2019;45:3192–8. http://dx.doi.org/10.1016/J.CERAMINT.2018.10.221.
[59] Gutiérrez CA, Moreno R. Tape casting of non-aqueous silicon nitride slips. J Eur Ceram Soc 2000;20:1527–37. http://dx.doi.org/10.1016/S0955-2219(99)00216-2.
[60] Pitchumani R, Karbhari VM. Generalized fluid flow model for ceramic tape casting. J Am Ceram Soc 1995;78:2497–503. http://dx.doi.org/10.1111/J.1151-2916.1995.TB08691.X.

[61] Chowdhury S, Lin Y, Liaw B, Kerby L. Evaluation of tree based regression over multiple linear regression for non-normally distributed data in battery performance. In: 2022 international conference on intelligent data science technologies and applications. Institute of Electrical and Electronics Engineers Inc.; 2022, p. 17–25. http://dx.doi.org/10.1109/IDSTA55301.2022.9923169.

[62] Importance of feature scaling. 2025, https://scikit-learn.org/stable/auto_examples/preprocessing/plot_scaling_importance.html. [Accessed 07 July 2025].

[63] Geron A. Hands-on machine learning with scikit-learn, keras, and tensorFlow: Concepts, tools, and techniques to build intelligent systems. 2nd ed. O'Reilly Media, Inc.; 2019.

[64] Zanotto FM, Dominguez DZ, Ayerbe E, Boyano I, Burmeister C, Duquesnoy M, Eisentraeger M, Montaño JF, Gallo-Bueno A, Gold L, Hall F, Kaden N, Muerkens B, Otaegui L, Reynier Y, Stier S, Thomitzek M, Turetskyy A, Vallin N, Wessel J, Xu X, Abbasov J, Franco AA. Data specifications for battery manufacturing digitalization: Current status, challenges, and opportunities. Batter Supercaps 2022;5:e202200224. http://dx.doi.org/10.1002/BATT.202200224.

[65] Troncoso JF, Zanotto FM, Galvez-Aranda DE, Dominguez DZ, Denisart L, Franco AA. The ARTISTIC battery manufacturing digitalization initiative: From fundamental research to industrialization. Batter Supercaps 2025;8:e202400385. http://dx.doi.org/10.1002/BATT.202400385.

[66] Xu K, Li Y, Liu C, Liu X, Hao X, Gao J, Maropoulos PG. Advanced data collection and analysis in data-driven manufacturing process. Chin J Mech Eng 2020 33:1 2020;33:1–21. http://dx.doi.org/10.1186/S10033-020-00459-X.